

A Tapered Gridded Estimator (TGE) for the Multi-Frequency Angular Power Spectrum (MAPS) and the Cosmological HI 21-cm Power Spectrum

Somnath Bharadwaj^{1*}, Srijita Pal¹, Samir Choudhuri² and Prasun Dutta³

¹ *Department of Physics, & Centre for Theoretical Studies, IIT Kharagpur, Kharagpur 721 302, India*

² *National Centre For Radio Astrophysics, Post Bag 3, Ganeshkhind, Pune 411007, India*

³ *Department of Physics, IIT (BHU), Varanasi 221005, India*

ABSTRACT

In this work we present a new approach to estimate the power spectrum $P(\mathbf{k})$ of redshifted HI 21-cm brightness temperature fluctuations. The MAPS $C_\ell(\nu_a, \nu_b)$ completely quantifies the second order statistics of the sky signal under the assumption that the signal is statistically homogeneous and isotropic on the sky. Here we generalize an already existing visibility based estimator for C_ℓ , namely TGE, to develop an estimator for $C_\ell(\nu_a, \nu_b)$. The 21-cm power spectrum is the Fourier transform of $C_\ell(\Delta\nu)$ with respect to $\Delta\nu = |\nu_a - \nu_b|$, and we use this to estimate $P(\mathbf{k})$. Using simulations of 150 MHz GMRT observations, we find that this estimator is able to recover $P(k)$ with an accuracy of 5 – 20% over a reasonably large k range even when the data in 80% randomly chosen frequency channels is flagged.

Key words: methods: statistical, data analysis - techniques: interferometric-cosmology: diffuse radiation

1 INTRODUCTION

Measurements of the cosmological HI 21-cm power spectrum can be used to probe the large scale distribution of neutral hydrogen (HI) across a large redshift range from the Dark Ages to the Post-Reionization Era (e.g. Bharadwaj & Ali 2005; Furlanetto, Oh & Briggs. 2006;

* Email:somnath@phy.iitkgp.ac.in

Morales & Wyithe 2010; Prichard & Loeb 2012; Mellema et al. 2013). Being very faint in nature, the 21-cm signal is buried in foregrounds which are four to five orders of magnitude larger than the expected signal (Shaver et al. 1999; Santos et al. 2005; Ali, Bharadwaj & Chengalur 2008; Bernardi et al. 2009; Ghosh et al. 2012; Iacobelli et al. 2013; Choudhuri et al. 2017a). There are several ongoing and future experiments, e.g. Donald C. Backer Precision Array to Probe the Epoch of Reionization (PAPER¹, Parsons et al. 2010), the Low Frequency Array (LOFAR², var Haarlem et al. 2013; Yatawatta et al. 2013), the Murchison Wide-field Array (MWA³, Bowman et al. 2013; Tingay et al. 2013), the Giant Metrewave Radio Telescope (GMRT, Swarup et al. 1991) the Square Kilometer Array (SKA1 LOW⁴, Koopmans et al. 2015) and the Hydrogen Epoch of Reionization Array (HERA⁵, DeBoer et al. 2017) which are aiming to detect the 21-cm power spectrum from the Epoch of Reionization (EoR).

The biggest challenge for a detection of the redshifted 21-cm signal are the foregrounds which include point sources, the diffuse Galactic synchrotron emission, the free-free emission from our Galaxy and external galaxies. Various techniques have been proposed to overcome this issue. The foreground subtraction technique proposes to subtract a foreground model from the visibility data or the image and use the residual data to detect the 21-cm power spectrum (Jelić et al. 2008; Bowman et al. 2009; Paciga et al. 2011; Chapman et al. 2012; Trott et al. 2012; Paciga et al. 2013; Trott et al. 2016). Considering $P(k_{\perp}, k_{\parallel})$, the cylindrical power spectrum of the 21-cm brightness temperature fluctuations, the foregrounds are expected to be primarily confined to a wedge in the $(k_{\perp}, k_{\parallel})$ plane. Here, k_{\perp} and k_{\parallel} refer to the components of the 3-dimensional wave vector \mathbf{k} perpendicular and parallel to the line of sight direction respectively. The foreground avoidance technique proposes to use the region outside this “Foreground Wedge” to estimate the 21-cm power spectrum (Datta et al. 2010; Parsons et al. 2012; Vedantham et al. 2012; Pober et al. 2013; Thyagarajan et al. 2013; Parsons et al. 2014; Pober et al. 2014; Liu et al. 2014a,b; Dillon et al. 2014, 2015; Ali et al. 2015).

A large variety of estimators have been proposed and applied to measure the power spectrum of the brightness temperature fluctuations using the visibility data measured in radio interferometric observations. Image-based estimators (Seljak 1997; Paciga et al. 2013) have

¹ <http://astro.berkeley.edu/dbacker/eor>

² <http://www.lofar.org/>

³ <http://www.mwatelescope.org>

⁴ <http://www.skatelescope.org/>

⁵ <http://reionization.org/>

the deconvolution error which arises during image reconstruction, and this may affect the estimated power spectrum. There are a few other techniques, like the Optimal Mapmaking Formalism (Morales & Matejek 2009) where the deconvolution errors can be avoided during imaging. It is possible to overcome this issue by estimating the power spectrum directly from the measured visibilities (Morales 2005; McQuinn, Zahn, Zaldarriaga, Hernquist & Furlanetto 2006; Pen, et al. 2009; Liu & Tegmark 2012; Parsons et al. 2012; Liu et al. 2014a,b; Dillon et al. 2015; Trott et al. 2016). Liu et al. (2016) have proposed an estimator which uses the spherical Fourier-Bessel basis to account for sky curvature. In addition to the sky signal, the visibilities (or the image) also have a noise contribution, and the noise bias is an important issue for power spectrum estimation. For example, Ali et al. (2015) have divided the data sets into even and odd LST bins and have correlated these to avoid introducing a noise bias. This approach however does not utilize the full signal available in the data. The foreground contributions from the outer regions of the telescope’s field of view (including the side-lobes) pose a severe problem for detecting the cosmological 21-cm signal (Pober et al. 2016). In this paper we develop on the visibility based Tapered Gridded Estimator (TGE; Choudhuri et al. 2014, Choudhuri et al. 2016b, hereafter Papers I and II respectively) whose salient features we summarize as follows. First, it uses the data to internally estimate the noise bias and subtracts this out to provide an unbiased estimate of the power spectrum. Second, it deals with the gridded visibilities which makes it computationally efficient. Third, it tapers the sky response to suppress the contribution from the outer regions of the telescope’s field of view.

Nearly all the estimators for $P(k_{\perp}, k_{\parallel})$, including the 3D TGE (Paper II), consider a Fourier transform of the measured visibilities $\mathcal{V}(\mathbf{U}, \nu)$ along the frequency axis ν to obtain the visibilities $\mathcal{V}(\mathbf{U}, \tau)$ in delay space τ (Morales & Hewitt 2004). This is used to estimate $P(k_{\perp}, k_{\parallel})$. A difficulty arises if the data is missing or flagged in a few frequency channels in which case the delay channel visibilities $\mathcal{V}(\mathbf{U}, \tau)$ and the estimated power spectrum $P(k_{\perp}, k_{\parallel})$ are both modified by a convolution with the Fourier transform of the frequency sampling function. Missing or flagged channels are quite common in any typical observation due to a variety of reasons including man made radio frequency interference (RFI). The CHIPS estimator developed by Trott et al. (2016) overcomes this problem by using Least-Squares Spectral Analysis (LSSA) to evaluate $\mathcal{V}(\mathbf{U}, \tau)$. However this needs to be applied individually for each baseline, and the entire process could be computationally expensive for large data volumes. In this paper we propose an alternative approach to estimate $P(k_{\perp}, k_{\parallel})$ which is

able to handle the problem of missing or flagged data with relative ease. Another point to note is that the earlier estimators all introduce a frequency filter which smoothly goes to zero at the two edges of the frequency band. This is introduced to avoid a discontinuity at the edges of the band, however it results in the loss of some signal. Such a filter is not needed in the new estimator proposed here.

The multi-frequency angular power spectrum $C_\ell(\nu_a, \nu_b)$ (MAPS; [Datta et al. 2007](#), [Mondal et al. 2018](#)) completely quantifies the second order statistics of the sky signal under the assumption that the signal is statistically homogeneous and isotropic on the sky. This however does not assume that the signal is ergodic or statistically homogeneous along the frequency axis. We have $C_\ell(\nu_a, \nu_b) = C_\ell(\Delta\nu)$ where $\Delta\nu = |\nu_a - \nu_b|$ if we impose the additional condition that the signal is ergodic along frequency. The 3D 21-cm power spectrum $P(k_\perp, k_\parallel)$ is the Fourier transform of $C_\ell(\Delta\nu)$. In the new approach presented here we first estimate $C_\ell(\Delta\nu)$ and use the binned $C_\ell(\Delta\nu)$ to estimate $P(k_\perp, k_\parallel)$. Even if some channels are missing, it is quite possible that the frequency separations $\Delta\nu$ are all present in the data. In this case it is quite straight forward to evaluate $P(k_\perp, k_\parallel)$ through a Fourier transform of $C_\ell(\Delta\nu)$. More sophisticated techniques like the LSSA can be used in case some $\Delta\nu$ are missing, however this needs to be applied to the binned $C_\ell(\Delta\nu)$ and the task is not computationally expensive.

The MAPS $C_\ell(\Delta\nu)$ has been used to quantify the statistical properties of the background radiation in GMRT observations at 150 MHz ([Ali, Bharadwaj & Chengalur 2008](#); [Ghosh et al. 2012](#)) and 610 MHz ([Ghosh et al. 2011a,b](#)). The HI signal contribution to the measured $C_\ell(\Delta\nu)$ is expected to decorrelate rapidly when $\Delta\nu$ is increased whereas the foreground contribution is expected to remain correlated for large $\Delta\nu$ separations. This property was used ([Ghosh et al. 2011b](#)) to model and remove the foreground contribution and obtain a residual $C_\ell(\Delta\nu)$ which is consistent with noise. It was thereby possible to place an observational limit on the HI 21-cm power spectrum at $z \approx 1.3$. The estimator used in these earlier works individually correlates pairs of visibilities to estimate $C_\ell(\Delta\nu)$, a technique which is computationally expensive. The 2D TGE (Paper II) presents an efficient technique to estimate the angular power spectrum C_ℓ . In Section 2. of this paper we have generalized this earlier work to develop an estimator for the MAPS $C_\ell(\nu_a, \nu_b)$. In Section 3. we present how $P(k_\perp, k_\parallel)$ is obtained from the estimated $C_\ell(\Delta\nu)$. Section 4. presents the Simulations which we have used to validate our estimator, Section 5. presents the Results and Section 6. presents the Discussion and Conclusions.

We have used the cosmological parameters from the (Planck + WMAP) best-fit Λ CDM cosmology (Planck Collaboration, P. A. R. Ade et al. 2015) throughout this paper.

2 AN OVERVIEW OF THE TAPERED GRIDDED ESTIMATOR

The 2D TGE, presented in Paper II considers radio-interferometric observations at a single frequency ν and uses the measured visibilities \mathcal{V}_i to estimate the angular power spectrum C_ℓ of the background radiation at the frequency ν . Here \mathcal{V}_i refers to the i -th visibility measurement with a corresponding baseline \mathbf{U}_i . The measured visibilities can be expressed as

$$\mathcal{V}_i = \left(\frac{\partial B}{\partial T} \right) \int d^2U \tilde{a}(\mathbf{U}_i - \mathbf{U}) \Delta \tilde{T}(\mathbf{U}) + \mathcal{N}_i. \quad (1)$$

Here, the first term is the sky signal which is the convolution of $\tilde{a}(\mathbf{U})$ and $\Delta \tilde{T}(\mathbf{U})$ where these are the Fourier transforms of the primary beam $\mathcal{A}(\boldsymbol{\theta})$ and the temperature fluctuations in the sky $\delta T(\boldsymbol{\theta})$ respectively, and $B = 2k_B T / \lambda^2$ is the Planck function in the Rayleigh-Jeans limit. The second term \mathcal{N}_i is the system noise contribution.

In order to taper the sky response, the measured visibilities are convolved with a function $\tilde{w}(\mathbf{U})$ which is the Fourier transform of a window function $\mathcal{W}(\boldsymbol{\theta})$ which falls off to a value close to zero well before the first null of the telescope’s primary beam pattern (Paper I). Further, in order to reduce the computation, the convolved visibilities are evaluated on a grid in uv space using

$$\mathcal{V}_{cg} = \sum_i \tilde{w}(\mathbf{U}_g - \mathbf{U}_i) \mathcal{V}_i. \quad (2)$$

where the ‘c’ in \mathcal{V}_{cg} refers to “convolved” and g refers to different grid points with corresponding baselines \mathbf{U}_g . The sky response of \mathcal{V}_{cg} is tapered with the window function $\mathcal{W}(\boldsymbol{\theta})$. Here we have used $\mathcal{W}(\boldsymbol{\theta}) = e^{-\theta^2/\theta_w^2}$ where the value of $\theta_w = 57'$ is chosen so as to suppress the contribution from the outer regions and sidelobes of the telescope’s primary beam pattern (Figure 1 of Choudhuri et al. 2016a). For comparison, the full width half maxima of the 150 MHz GMRT primary beam pattern may be estimated to be $1.03\lambda/D = 157'$ where $D = 45$ m is the antenna diameter.

The convolved gridded visibilities can be expressed as

$$\mathcal{V}_{cg} = \left(\frac{\partial B}{\partial T} \right) \int d^2U \tilde{K}(\mathbf{U}_g - \mathbf{U}) \Delta \tilde{T}(\mathbf{U}) + \sum_i \tilde{w}(\mathbf{U}_g - \mathbf{U}_i) \mathcal{N}_i, \quad (3)$$

where

$$\tilde{K}(\mathbf{U}_g - \mathbf{U}) = \int d^2U' \tilde{w}(\mathbf{U}_g - \mathbf{U}') B(\mathbf{U}') \tilde{a}(\mathbf{U}' - \mathbf{U}) \quad (4)$$

is an effective “gridding kernel”, and

$$B(\mathbf{U}) = \sum_i \delta_D^2(\mathbf{U} - \mathbf{U}_i) \quad (5)$$

is the baseline sampling function of the measured visibilities.

The 2D TGE estimator is defined as

$$\hat{E}_g = M_g^{-1} \left(|\mathcal{V}_{cg}|^2 - \sum_i |\tilde{w}(\mathbf{U}_g - \mathbf{U}_i)|^2 |\mathcal{V}_i|^2 \right). \quad (6)$$

with $\langle \hat{E}_g \rangle = C_{\ell_g}$ where $\ell_g = 2\pi U_g$, and $\langle \rangle$ denotes an ensemble average over multiple realizations of the sky brightness temperature fluctuations which are recorded in the visibilities. The second term in the brackets (...) in eq. (6) is introduced to subtract out the noise bias contribution which arises due to the correlation of a visibility with itself. M_g is a normalization factor which we shall discuss later. Simulations show that the 2D TGE provides an unbiased estimate of the angular power spectrum C_ℓ (Paper II) while effectively suppressing the contribution from the sidelobes and outer regions of the telescope’s primary beam (Choudhuri et al. 2017b).

2.1 M_g Calculation

As discussed in Paper II, the normalization constant M_g can be written as,

$$M_g = V_{1g} - \sum_i |\tilde{w}(\mathbf{U}_g - \mathbf{U}_i)|^2 V_0 \quad (7)$$

where,

$$V_{1g} = \left(\frac{\partial B}{\partial T} \right)^2 \int d^2U |\tilde{K}(\mathbf{U}_i - \mathbf{U})|^2. \quad (8)$$

and

$$V_0 = \left(\frac{\partial B}{\partial T} \right)^2 \int d^2U |\tilde{a}(\mathbf{U}_i - \mathbf{U})|^2. \quad (9)$$

The values of M_g (eq. 7) depend on the baseline distribution (eq. 5) and the form of the tapering function $\mathcal{W}(\theta)$, and it is necessary to calculate M_g at every grid point in the uv plane. Paper I presents an analytic approximation to estimate M_g . While this has been found to work very well in a situation where the baselines have a nearly uniform and dense uv coverage (Fig. 7 of Paper I), it leads to C_ℓ being overestimated in a situation where we have a sparse and non-uniform uv coverage. Paper II presents a different method to estimate M_g which has been found to work well even if the uv coverage is sparse and non-uniform .

We now briefly present how the normalization constant M_g is calculated for C_ℓ estimation in eq. (6). As discussed in Paper II, we proceed by constructing random realizations of simulated visibilities $[\mathcal{V}_i]_{\text{UPAS}}$ corresponding to a situation where the sky signal has an unit angular power spectrum (UAPS) $C_\ell = 1$. The simulated visibilities have exactly the same baseline distribution as the actual observed visibilities. We then have (eq. 6)

$$M_g = \left\langle \left(|\mathcal{V}_{cg}|^2 - \sum_i |\tilde{w}(\mathbf{U}_g - \mathbf{U}_i)|^2 \langle |\mathcal{V}_i|^2 \rangle \right) \right\rangle_{\text{UPAS}} \quad (10)$$

which allows us to estimate M_g . We average over N_u independent realizations of the UPAS to reduce the statistical uncertainty.

2.2 Binning

The estimator \hat{E}_g provides an estimate of C_ℓ at different grid points \mathbf{U}_g on the uv plane. We have binned the estimates in order to increase the signal to noise ratio and also reduce the data volume. The signal is assumed to be statistically isotropic on the sky whereby it is independent of the direction of \mathbf{U}_g . This allows us to average the C_ℓ estimates within an annular region on the uv plane. We define the binned Tapered Gridded Estimator for bin a using

$$\hat{E}_G(a) = \frac{\sum_g w_g \hat{E}_g}{\sum_g w_g}. \quad (11)$$

where w_g refers to the weight assigned to the contribution from any particular grid point. The choice $w_g = 1$ assigns equal weightage to the value of C_{ℓ_g} estimated at each grid point, whereas $w_g = M_g$ corresponds to a situation where the grid points which have a denser baseline sampling (less system noise) would be given a larger weightage. The former would be desirable if one wishes to optimize with respect to the cosmic variance whereas the latter would be preferred to optimize with respect to the system noise contribution. The optimum choice of w_g to maximize the signal to noise ratio would depend on the window function and the baseline distribution, and we plan to address this in future.

The binned estimator has an expectation value

$$\bar{C}_{\bar{\ell}_a} = \frac{\sum_g w_g C_{\ell_g}}{\sum_g w_g} \quad (12)$$

where $\bar{C}_{\bar{\ell}_a}$ is the average angular power spectrum at

$$\bar{\ell}_a = \frac{\sum_g w_g \ell_g}{\sum_g w_g} \quad (13)$$

which is the effective angular multipole for bin a .

3 THE MULTI-FREQUENCY ANGULAR POWER SPECTRUM

The multi-frequency angular power spectrum $C_\ell(\nu_a, \nu_b)$ (Datta et al. 2007) characterizes the joint frequency and angular dependence of the statistical properties of the background sky signal. We decompose the brightness temperature fluctuations $\delta T_b(\hat{\mathbf{n}}, \nu)$ in terms of spherical harmonics $Y_\ell^m(\hat{\mathbf{n}})$ using

$$\delta T_b(\hat{\mathbf{n}}, \nu) = \sum_{\ell, m} a_{\ell m}(\nu) Y_\ell^m(\hat{\mathbf{n}}) \quad (14)$$

and define the multi-frequency angular power spectrum (hereafter MAPS) as

$$C_\ell(\nu_a, \nu_b) = \langle a_{\ell m}(\nu_a) a_{\ell m}^*(\nu_b) \rangle. \quad (15)$$

As discussed in Mondal et al. (2018), we expect $C_\ell(\nu_1, \nu_2)$ to entirely quantify the second order statistics of the redshifted 21-cm signal.

We now proceed to define a visibility based Tapered Gridded Estimator (TGE) for $C_\ell(\nu_a, \nu_b)$. We generalize the analysis to consider visibility measurements $\mathcal{V}_i(\nu_a)$ at multiple frequency channels $1 \leq a \leq N_c$, each of width $\Delta\nu_c$, with N_c channels that span a bandwidth B_{bw} . Here we allow for the possibility that several of the data are bad or missing. We assume that such data has been identified and flagged, and this information is stored using a flagging variable $F_i(\nu_a)$ which has value 0 for the flagged data and value 1 otherwise. We then have

$$\mathcal{V}_{cg}(\nu_a) = \sum_i \tilde{w}(\mathbf{U}_g - \mathbf{U}_i) \mathcal{V}_i(\nu_a) F_i(\nu_a). \quad (16)$$

which allows us to define the Tapered Gridded Estimator (TGE) for $C_\ell(\nu_a, \nu_b)$ as

$$\hat{E}_g(\nu_a, \nu_b) = M_g^{-1}(\nu_a, \nu_b) \mathcal{Re} \left(\mathcal{V}_{cg}(\nu_a) \mathcal{V}_{cg}^*(\nu_b) - \delta_{a,b} \sum_i F_i(\nu_a) |\tilde{w}(\mathbf{U}_g - \mathbf{U}_i)|^2 |\mathcal{V}_i(\nu_a)|^2 \right). \quad (17)$$

where $\mathcal{Re}()$ denotes the real part, $\delta_{a,b}$ is a Kronecker delta *i.e.* it is necessary to subtract the noise bias only when the two frequencies are the same ($\nu_a = \nu_b$), and the noise in the visibility measurements at two different frequencies ($\nu_a \neq \nu_b$) are uncorrelated.

The TGE defined in eq. (17) provides an unbiased estimate of $C_{\ell_g}(\nu_a, \nu_b)$ at the angular multipole $\ell_g = 2\pi U_g$ *i.e.*

$$\langle \hat{E}_g(\nu_a, \nu_b) \rangle = C_{\ell_g}(\nu_a, \nu_b) \quad (18)$$

We use this to define the binned Tapered Gridded Estimator for bin a

$$\hat{E}_G[a](\nu_a, \nu_b) = \frac{\sum_g w_g \hat{E}_g(\nu_a, \nu_b)}{\sum_g w_g}. \quad (19)$$

where w_g refers to the weight assigned to the contribution from any particular grid point g .

For the analysis presented in this paper we have used the weight $M_g(\nu_a, \nu_b)$ which roughly averages the visibility correlation $\mathcal{V}_{cg}(\nu_a) \mathcal{V}_{cg}^*(\nu_b)$ across all the grid points which are sampled by the baseline distribution. The binned estimator has an expectation value

$$\bar{C}_{\bar{\ell}_a}(\nu_a, \nu_b) = \frac{\sum_g w_g C_{\ell_g}(\nu_a, \nu_b)}{\sum_g w_g} \quad (20)$$

where $\bar{C}_{\bar{\ell}_a}(\nu_a, \nu_b)$ is the bin averaged multi-frequency angular power spectrum (MAPS) at

$$\bar{\ell}_a = \frac{\sum_g w_g \ell_g}{\sum_g w_g} \quad (21)$$

which is the effective angular multipole for bin a .

Paper II describes how we have estimated M_g using UAPS simulations in the context of observations at a single frequency. This has also been summarized in Section 2 of this paper. Here we have extended the earlier analysis to simulate visibilities $[\mathcal{V}_i(\nu_a)]_{\text{UMAPS}}$ for which we have an unit multi-frequency angular power spectrum $C_\ell(\nu_a, \nu_b) = 1$. We also apply the same flagging variable $F_i(\nu_a)$ as the actual data to the simulated data. Using the simulated visibilities $[\mathcal{V}_i(\nu_a)]_{\text{UMAPS}}$ and the actual flagging variable $F_i(\nu_a)$ in eq. (17), we have an estimate of $M_g(\nu_a, \nu_b)$. We have used multiple realizations of the simulations to reduce the uncertainty in the estimated values of $M_g(\nu_a, \nu_b)$.

We note that the estimator presented here does not take into account the fact that the baselines $\mathbf{U}_i = \mathbf{d}_i/\lambda$ (where \mathbf{d} is the antenna spacing) and the primary beam pattern $\mathcal{A}(\boldsymbol{\theta}, \nu)$ both change with frequency and these are held fixed at the values corresponding to the central frequency ν_c . While this may not have a very significant effect on the recovered 21-cm power spectrum, it is very important for the foregrounds where this leads to the foreground wedge (eg. Datta et al. 2010; Parsons et al. 2012; Vedantham et al. 2012). We note that the frequency dependence of the baselines has been included in earlier versions of the MAPS estimator (Ali, Bharadwaj & Chengalur 2008; Ghosh et al. 2011a, 2012) which did not incorporate gridding and tapering. It is possible to incorporate the frequency dependence of the baselines in the TGE by suitably scaling the baselines \mathbf{U}_i at the time of convolution and gridding (eq. 16), and we plan to address this in future work.

4 ESTIMATING $P(K_\perp, K_\parallel)$

In order to estimate the 3D power spectrum $P(k_\perp, k_\parallel)$ we assume that the redshifted 21-cm signal is statistically homogeneous (ergodic) along the line of sight (e.g. Mondal et al. 2018). We then have $C_\ell(\nu_a, \nu_b) = C_\ell(\Delta\nu)$ where $\Delta\nu = |\nu_b - \nu_a|$ *i.e.* the statistical properties of

the signal depends only on the frequency separation and not the individual frequencies. In the flat sky approximation, the power spectrum $P(k_{\perp}, k_{\parallel})$ of the brightness temperature fluctuations of the redshifted 21-cm signal is the Fourier transform of $C_{\ell}(\Delta\nu)$, and we have (Datta et al. 2007)

$$P(k_{\perp}, k_{\parallel}) = r^2 r' \int_{-\infty}^{\infty} d(\Delta\nu) e^{-ik_{\parallel}r'\Delta\nu} C_{\ell}(\Delta\nu) \quad (22)$$

where k_{\parallel} and $k_{\perp} = \ell/r$ are the components of \mathbf{k} respectively parallel and perpendicular to the line of sight, r is the comoving distance corresponding to ν_c the central frequency of our observations and $r' (= dr/d\nu)$ is evaluated at ν_c . A brief derivation of eq. (22) is also presented in the Appendix of Mondal et al. (2018). In this paper we have used (eq. 22) to estimate $P(k_{\perp}, k_{\parallel})$ from the MAPS $C_{\ell}(\nu_a, \nu_b)$.

First we impose the ergodic assumption on $C_{\ell}(\nu_a, \nu_b)$ which has been estimated from the visibility data using eq. (17) and binned using eq. (19,20 and 21). For a fixed ℓ and $\Delta\nu$, we average over all the $C_{\ell}(\nu_a, \nu_b)$ values for which $|\nu_b - \nu_a| = \Delta\nu$ to obtain $C_{\ell}(\Delta\nu)$. We then have $C_{\ell}(n\Delta\nu_c)$ where $-(N_c - 1) \leq n \leq (N_c - 1)$ with $C_{\ell}(n\Delta\nu_c) = C_{\ell}(-n\Delta\nu_c)$. We see that $C_{\ell}(n\Delta\nu_c)$ is a periodic function of n with period $2N_c - 2$. We use the discrete Fourier transform

$$\bar{P}(k_{\perp}, k_{\parallel m}) = (r^2 r' \Delta\nu_c) \sum_{n=-N_c+2}^{N_c-1} \exp(-ik_{\parallel m}r'n\Delta\nu_c) C_{\ell}(n\Delta\nu_c) \quad (23)$$

with $k_{\parallel m} = m \times [\pi/r'_c \Delta\nu_c (N_c - 1)]$ to estimate $\bar{P}(k_{\perp}, k_{\parallel m})$ which is already binned in k_{\perp} . We have further binned in $k_{\parallel m}$ to obtain the Spherical Power Spectrum $P(k)$, and the Cylindrical Power Spectrum $P(k_{\perp}, k_{\parallel})$.

5 SIMULATIONS

We have carried out simulation to validate the estimator presented here. We have simulated 8 hours of 150 MHz Giant Meterwave Radio Telescope (Swarup et al. 1991) observations with $N_c = 257$ channels of width $\Delta\nu_c = 62.5$ KHz spanning $B_{bw} \approx 16$ MHz and integration time $\Delta t = 16$ s towards RA=10h46m00s and DEC=59°00'59". We note that the EoR 21-cm signal is not expected to be ergodic over the 16 MHz bandwidth considered here due to the Light Cone effect (Mondal et al. 2018). However, we have not considered this effect here and assumed that the signal is ergodic. The sky signal, we assume, is entirely the redshifted HI 21-cm emission whose brightness temperature fluctuations are characterized by the 3D power spectrum $P^m(k) = (k/k_0)^n \text{mK}^2 \text{Mpc}^3$. For the purpose of this paper we have arbitrarily

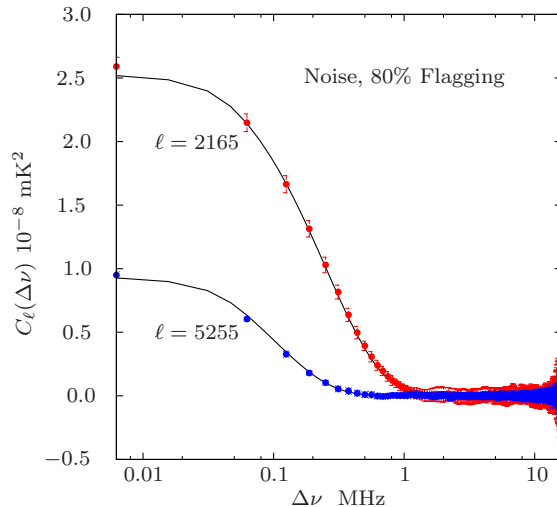


Figure 1. This shows $C_\ell(\Delta\nu)$ as a function of $\Delta\nu$ for two values of ℓ . The data points with $1 - \sigma$ error-bars are estimated from 24 realizations of the simulations. Note that the $\Delta\nu = 0$ points have been slightly shifted for convenience of plotting on a logarithmic scale. The lines show the theoretical predictions calculated by using the input model power spectrum $P^m(k)$ in eq. (24).

chosen the values $k_0 = (1.1)^{-1/2} \text{Mpc}^{-1}$ and $n = -2$. We have followed the procedure outlined in Section 4 of Choudhuri et al. (2016b) to simulate visibilities $\mathcal{V}_i(\nu_a)$ corresponding to different statistically independent realizations of the brightness temperature fluctuations.

In addition to the sky signal, the visibilities also contain a system noise contribution. We have modelled the system noise contribution to the visibilities as Gaussian random variables whose real and imaginary parts both have zero mean and variance σ_N^2 . For comparison we have also estimated σ_{sky}^2 which is the same quantity for the simulated sky signal contribution. The ratio $R = \sigma_N/\sigma_{sky}$ gives an estimate of the relative contribution of the system noise with respect to the sky signal. In our simulations we have used $R = 10$ which corresponds to a situation where the noise contribution to an individual visibility is $R = 10$ times the sky signal contribution. We have generated 24 statistically independent realizations of both the sky signal and the system noise. The resulting 24 statistically independent realizations of the simulated visibilities were used to estimate the mean and $1 - \sigma$ errors for the results presented below. We have considered simulations both with and without flagging. For each baseline we have generated random integers in the range $1 \leq a \leq N_c$ and flagged the corresponding channels. We have carried out simulations for various values of f_{FLAG} (the fraction of flagged channels) in the range $0 \leq f_{\text{FLAG}} \leq 0.8$.

We note that the frequency dependence of the baselines $\mathbf{U} = \mathbf{d}/\lambda$ and the primary beam pattern $\mathcal{A}(\boldsymbol{\theta}, \nu)$ have both been incorporated in the simulated visibilities.

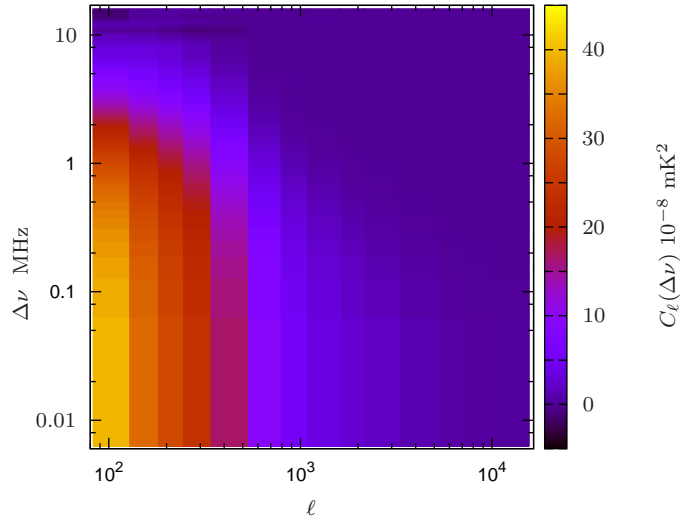


Figure 2. This shows $C_\ell(\Delta\nu)$ across the entire ℓ and $\Delta\nu$ range considered here for simulations with noise and 80% flagging. We have shifted the $\Delta\nu = 0$ values to $\Delta\nu = 0.006251\text{MHz}$ for convenience of plotting on a logarithmic scale.

6 RESULTS

The analysis here was restricted to baselines in the range $10 \leq |\mathbf{U}_i| \leq 3,000$, and the uv plane was divided into 15 annular bins at equal logarithmic intervals for power spectrum estimation. This corresponds to the k_\perp range $7 \times 10^{-3} \text{Mpc}^{-1}$ to 2.03Mpc^{-1} . Figure 1 shows the binned power spectrum $C_\ell(\Delta\nu)$ at two different values of ℓ considering simulations with noise and 80% flagging. For comparison we have also shown the theoretical prediction corresponding to the input model power spectrum $P^m(k)$ calculated using

$$C_\ell(\Delta\nu) = \frac{1}{\pi r^2} \int_0^\infty dk_\parallel \cos(k_\parallel r' \Delta\nu) P(k_\perp, k_\parallel) \quad (24)$$

which is the inverse of eq. (22). We see that the results from the simulations are in agreement with the theoretical predictions. The results shown here are visually indistinguishable from the results from simulations with no noise and no flagging, or those with 20%, 40% and 60% flagging, and we have not shown the other results here.

We find that the value of $C_\ell(\Delta\nu)$ falls rapidly as $\Delta\nu$ is increased, and it has a value close to zero for $\Delta\nu > 1 \text{MHz}$. Considering the simulations with noise and 80% flagging, Figure 2 provides a visual representation of $C_\ell(\Delta\nu)$ across the entire ℓ and $\Delta\nu$ range that we have considered here. The results are visually indistinguishable even if we have no noise and no flagging (or less flagging), or if we evaluate $C_\ell(\Delta\nu)$ analytically using (eq. 24) and we have not shown these here. We see that the value of $C_\ell(\Delta\nu)$ decrease as ℓ is increased. For a fixed ℓ , the value of $C_\ell(\Delta\nu)$ falls rapidly as $\Delta\nu$ is increased and it has a value close to zero at large

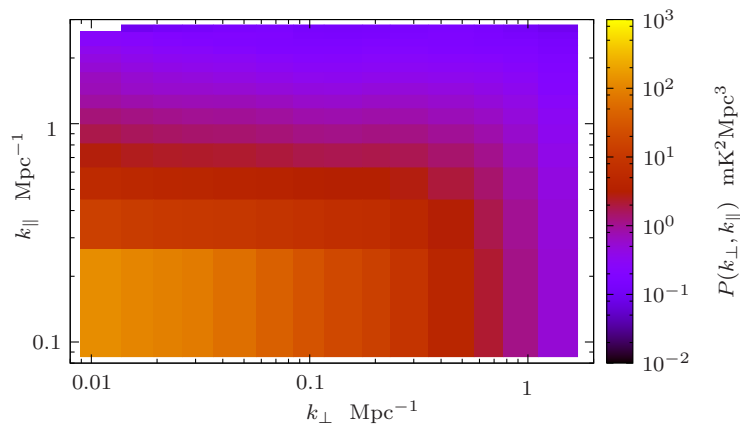


Figure 3. The cylindrical power spectrum $P(k_{\perp}, k_{\parallel})$ estimated from simulations with noise and 80% flagging.

$\Delta\nu$. The decrease in the value of $C_{\ell}(\Delta\nu)$ with increasing $\Delta\nu$ is more rapid as we go to larger ℓ . The behaviour of $C_{\ell}(\Delta\nu)$ is directly manifested in the visibility correlation $V_2(U, \Delta\nu) = \langle \mathcal{V}^*(\mathbf{U}, \nu) \mathcal{V}(\mathbf{U}, \nu + \Delta\nu) \rangle$ with $\ell = 2\pi U$. This has been studied extensively in several earlier works (Bharadwaj & Sethi 2001; Bharadwaj & Pandey 2003; Bharadwaj & Ali 2005), and we do not discuss this any further here.

Figure 3 shows the cylindrical power spectrum $P(k_{\perp}, k_{\parallel})$ estimated by applying eq. (23) to the $C_{\ell}(\Delta\nu)$ obtained from the simulations with noise and 80% flagging (Figure 2). We obtain estimates of $P(k_{\perp}, k_{\parallel})$ in 15 bins of equal logarithmic spacing along k_{\perp} each with $N_c = 257$ values along k_{\parallel} . We have further binned $P(k_{\perp}, k_{\parallel})$ into 16 bins of equal logarithmic spacing along k_{\parallel} to increase the signal to noise ratio and also for convenience of plotting. The results for the other cases which we have considered (lesser flagging, with/without noise) are very similar and they have not been shown separately. Note that the estimated power spectrum turns out to be negative at a single pixel (top left corner of the figure) when we have 80% flagging. In contrast, we obtain positive values at all the pixels when we consider a smaller percentage of flagged data.

The upper panel of Figure 4 shows the spherical power spectrum $P(k)$ estimated from the simulations with no noise and no flagging, and also the simulations with noise and 80% flagging. Here the $P(k_{\perp}, k_{\parallel})$ values were combined into 15 bins of equal logarithmic interval in the k range $4 \times 10^{-3} \text{ Mpc}^{-1}$ to 3 Mpc^{-1} . We see that the results from these two sets of simulations are visually indistinguishable. The results for all the other cases considered here are very similar and they have not been shown separately. The model power spectrum $P^m(k)$

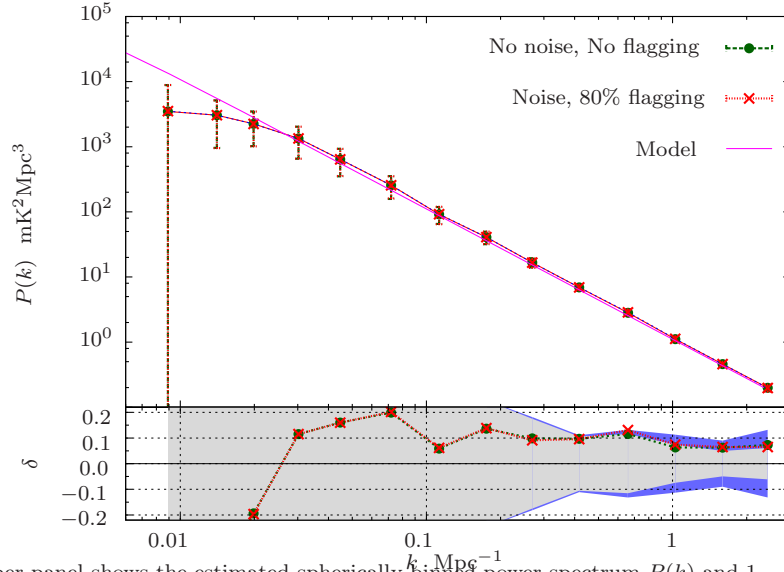


Figure 4. The upper panel shows the estimated spherically-binned power spectrum $P(k)$ and $1 - \sigma$ error-bars for simulations with no noise and flagging and also with noise and 80% flagging. For comparison, the input model $P^m(k)$ is also shown by the solid line. The bottom panel shows the fractional error $\delta = [P(k) - P^m(k)]/P^m(k)$ (data points) and the relative statistical fluctuation $\sigma/P^m(k)$ (shaded regions). The values of σ are larger for simulations with noise and 80% flagging as compared to those with no noise and no flagging.

is also shown for comparison. We see that $P(k)$ estimated from the simulations is below the model predictions at $k < 0.02 \text{ Mpc}^{-1}$. Our estimator assumes that the convolution due to the telescope’s primary beam pattern can be well approximated by a multiplicative factor which we have incorporated in M_g (eq. 17). Earlier studies (Choudhuri et al. 2014) show that this assumption does not hold at the small baselines (which also correspond to small k_{\perp}) that probe angular scales which are comparable to the angular extent of the telescope’s primary beam pattern. The estimated power spectrum is in better agreement with the input model at $k \geq 0.02 \text{ Mpc}^{-1}$. We however notice that $P(k)$ is somewhat overestimated at $k \geq 0.03 \text{ Mpc}^{-1}$, but this difference goes down at larger k . The lower panel shows the fractional deviation $\delta = [P(k) - P^m(k)]/P^m(k)$ of the estimated power spectrum $P(k)$ relative to the input model $P^m(k)$, the shaded regions shows the $1 - \sigma$ errors $\sigma/P^m(k)$. We find that $P(k)$ is overestimated by 10 – 20% in the range $0.03 \leq k < 0.1 \text{ Mpc}^{-1}$, this falls to 5 – 15% in the range $0.1 \leq k < 1.0 \text{ Mpc}^{-1}$ and the overestimate is less than 7.5% at $k > 1.0 \text{ Mpc}^{-1}$. There is around $\sim 1\%$ difference in the estimated values when we have noise and 80% flagging as compared to the situation when these are not incorporated. Further, the values of σ are larger when we introduce noise and flagging, this is particularly more pronounced at large k . In all cases we find that the errors δ are less than the expected statistical fluctuations $\sigma/P^m(k)$.

7 DISCUSSION AND CONCLUSIONS

The error-bars shown here are based on 24 independent realizations of the simulations. [Choudhuri et al. \(2014\)](#) and [Choudhuri et al. \(2016b\)](#) present analytical formulas for estimating the statistical errors, and it is possible to obtain similar formulas for $C_\ell(\nu_a, \nu_b)$ and propagate the resulting errors through the Fourier transform to predict errors for $P(\mathbf{k})$. However, simulations offer a more straight forward method to estimate the errors. It is possible to use the estimated power spectrum as an input for simulations, and use multiple realizations of these simulations to estimate the error-bars for the estimated power spectrum.

An earlier study ([Choudhuri et al. 2014](#)) used simulations to show that the TGE overestimates C_ℓ due to the sparse and patchy uv coverage of the GMRT baseline distribution. This overestimate was found to come down if a more dense and uniform uv coverage was considered instead. The estimator presented here overestimates $P(k)$ by 5 – 20% across a large portion of the k range, the exact cause for this is not known at present. We believe that this is a consequence of the sparse and patchy uv coverage of the GMRT baseline distribution, and is not an inherent limitation of the estimator. We expect this effect to be much less severe for an array with a denser and more uniform uv coverage. Further studies considering arrays with different uv coverage are needed to quantitatively establish this, and we propose to address this in future work.

The signal in the visibility measurements $\mathcal{V}(\mathbf{U}_i, \nu_a)$ at different baselines \mathbf{U}_i are not independent due to the telescope's primary beam pattern and the signal at baselines within D/λ are correlated (eq. (12) of [Bharadwaj & Ali 2005](#)) where D is the antenna diameter. Similarly, the visibility measurements $\mathcal{V}(\mathbf{U}_i, \nu_a)$ at different frequency channels ν_a are not independent (Figure 9 of [Bharadwaj & Ali 2005](#)) and the signal remains correlated across different channels, the width of the correlation depending on the value of \mathbf{U}_i ([Bharadwaj & Pandey 2003](#)). The signal contained in the flagged data which is lost is also contained in the valid data which is available at our disposal for power spectrum estimation, and the estimator presented here is able to recover the power spectrum equally well even if 80% of the data is flagged. While the estimated power spectrum is practically unchanged with or without flagging, the statistical fluctuations σ are somewhat larger (particularly at large k) when flagging is introduced. The entire analysis presented here is restricted to a situation where randomly chosen frequency channels were flagged. A variety of other situations may occur in real life. For a given real data it would be best to first use the flagging

variables of the actual data in conjunction with simulations to verify if the estimator can reproduce the input model of the simulation. If needed, the discrete Fourier transform of eq. (23) can be replaced by a more sophisticated spectral estimator. However, here it is necessary to apply this to the final binned data and not the individual baselines, and therefore the problem is not computationally demanding. We propose to address these issues in more detail in future work.

In a recent paper [Morales et al. \(2018\)](#) has broadly classified the power spectrum estimators into two classes namely (1.) the delay spectrum or measured sky estimators, and (2.) the reconstructed sky estimators. The former class of estimators performs the Fourier transform from ν to k_{\parallel} at a fixed antenna separation \mathbf{d} which does not incorporate the frequency dependence of the baseline. In contrast, the same Fourier transform is carried out at the baseline \mathbf{U} corresponding to a fixed angular scale which effectively incorporates the variation of baseline with frequency, however it uses a reconstructed sky model instead of the measured sky signal. The estimator presented here deals with the measured sky signal, it however differs from the usual delay spectrum estimators in that the signal is first correlated and then Fourier transformed. It is consequently possible to incorporate the frequency dependence of the baselines (as mentioned in Section 3). This has not been incorporated in the present work, we plan to incorporate this and study its impact on foregrounds in future work.

REFERENCES

- Ali S. S., Bharadwaj S., & Chengalur J. N., 2008, MNRAS, 385, 2166A
 Ali, Z. S., Parsons, A. R., Zheng, H., et al. 2015, ApJ, 809, 61
 Bernardi, G., de Bruyn, A. G., Brentjens, M. A., et al. 2009, A&A, 500, 965
 Bharadwaj, S. & Sethi, S. K., 2001, JApA, 22, 293
 Bharadwaj, S., & Pandey, S. K. 2003, JAPA, 24, 23.
 Bharadwaj S., & Ali S. S. 2005, MNRAS, 356, 1519
 Bowman, J. D., Morales, M. F., & Hewitt, J. N. 2009, ApJ, 695, 183
 Bowman J. D. et al., 2013, PASA, 30, e031
 Chapman, E., Abdalla, F. B., Harker, G., et al. 2012, MNRAS, 423, 2518
 Choudhuri, S., Bharadwaj, S., Ghosh, A., & Ali, S. S., 2014, MNRAS, 445, 4351
 Choudhuri, S., Bharadwaj, S., Roy, N., Ghosh, A., & Ali, S. S., 2016a, MNRAS, 459, 151
 Choudhuri, S., Bharadwaj, S., Chatterjee, S., et al. 2016b, MNRAS, 463, 4093
 Choudhuri, S., Bharadwaj, S., Ali, S. S., et al. 2017a, MNRAS, 470, L11
 Choudhuri, S., Roy, N., Bharadwaj, S., et al. 2017b, New Astron., 57, 94
 Datta, K. K., Choudhury, T. R., & Bharadwaj, S. 2007, MNRAS, 378, 119
 Datta, A., Bowman, J. D., & Carilli, C. L. 2010, ApJ, 724, 526

- DeBoer, D. R., Parsons, A. R., Aguirre, J. E., et al. 2017, *PASP*, 129, 045001
- Dillon, J. S., Liu, A., Williams, C. L., et al. 2014, *PRD*, 89, 023002
- Dillon, J. S., Liu, A., Williams, C. L., et al. 2015, *PRD*, 91(12), 123011
- Furlanetto S. R., Oh S. P., Briggs F. H., 2006, *Phys. Rep.*, 433, 181
- Ghosh, A., Bharadwaj, S., Ali, S. S., & Chengalur, J. N. 2011a, *MNRAS*, 411, 2426
- Ghosh, A., Bharadwaj, S., Ali, S. S., & Chengalur, J. N. 2011b, *MNRAS*, 418, 2584
- Ghosh, A., et al. 2012, *MNRAS*, 426, 3295
- Iacobelli, M., Haverkorn, M., Orrú, E., et al. 2013, *A&A*, 558, A72
- Jelić, V., Zaroubi, S., Labropoulos, P., et al. 2008, *MNRAS*, 389, 1319
- Koopmans, L., Pritchard, J., Mellema, G., et al. 2015, *Advancing Astrophysics with the Square Kilometre Array (AASKA14)*, 1
- Liu, A., & Tegmark, M. 2012, *MNRAS*, 419, 3491
- Liu, A., Parsons, A. R., & Trott, C. M. 2014a, *PRD*, 90, 023018
- Liu, A., Parsons, A. R., & Trott, C. M. 2014b, *PRD*, 90, 023019
- Liu, A., Zhang, Y., & Parsons, A. R. 2016, *ApJ*, 833, 242
- McQuinn M., Zahn O., Zaldarriaga M., Hernquist L., Furlanetto S. R., 2006, *ApJ*, 653, 815
- Mellema, G., et al. 2013, *Experimental Astronomy*, 36, 235
- Mondal, R., Bharadwaj, S., & Datta, K. K. 2018, *MNRAS*, 474, 1390
- Morales, M. F., & Hewitt, J. 2004, *ApJ*, 615, 7
- Morales M. F., 2005, *ApJ*, 619, 678
- Morales M. F., Matejek M., 2009, *MNRAS*, 400, 1814
- Morales, M. F., & Wyithe, J. S. B. 2010, *ARA&A*, 48, 127
- Morales M. F., Beardsley A., Pober J., Barry N., Hazelton B., Jacobs D., Sullivan I., 2018, *MNRAS*, 2715
- Paciga G. et al., 2011, *MNRAS*, 413, 1174
- Paciga, G., Albert, J. G., Bandura, K., et al. 2013, *MNRAS*, 433, 639
- Parsons A. R. et al., 2010, *AJ*, 139, 1468
- Parsons, A. R., Pober, J. C., Aguirre, J. E., et al. 2012, *ApJ*, 756, 165
- Parsons, A. R., Liu, A., Aguirre, J. E., et al. 2014, *ApJ*, 788, 106
- Pen U.-L., et al., 2009, *MNRAS*, 399, 181
- Planck Collaboration, P. A. R. Ade et al., Planck 2015 results. XIII. Cosmological parameters, arXiv:1502.01589.
- Poher J. C. et al., 2013, *ApJ*, 768, L36
- Poher, J. C., Liu, A., Dillon, J. S., et al. 2014, *ApJ*, 782, 66
- Poher, J. C., Hazelton, B. J., Beardsley, A. P., et al. 2016, arXiv:1601.06177
- Pritchard, J. R. and Loeb, A., 2012, *Reports on Progress in Physics* 75(8), 086901
- Santos, M.G., Cooray, A. & Knox, L. 2005, 625, 575
- Seljak, U. 1997, *ApJ*, 482, 6
- Shaver, P. A., Windhorst, R. A., Madau, P., & de Bruyn, A. G. 1999, *A&A*, 345, 380
- Swarup, G., Ananthakrishnan, S., Kapahi, V. K., Rao, A. P., Subrahmanya, C. R., and Kulkarni, V. K. 1991, *CURRENT SCIENCE*, 60, 95.
- Thyagarajan, N., Udaya Shankar, N., Subrahmanyan, R., et al. 2013, *ApJ*, 776, 6
- Thyagarajan, N., Jacobs, D. C., Bowman, J. D., et al. 2015, *ApJ*, 807, L28
- Tingay, S. et al. 2013, *Publications of the Astronomical Society of Australia*, 30, 7
- Trott, C. M., Wayth, R. B., & Tingay, S. J. 2012, *ApJ*, 757, 101
- Trott, C. M., Pindor, B., Procopio, P., et al. 2016, *ApJ*, 818, 139
- van Haarlem, M. P., Wise, M. W., Gunst, A. W., et al. 2013, *A&A*, 556, A2
- MNRAS 000, 000–000 (0000)

Vedantham, H., Udaya Shankar, N., & Subrahmanyan, R. 2012, *ApJ*, 745, 176

Yatawatta, S. et al. 2013, *Astronomy & Astrophysics*, 550, 136